GEOPHYSICS, VOL. 68, NO. 2 (MARCH-APRIL 2003); P. 705–717, 6 FIGS., 1 TABLE.
10.1190/1.1567241

Poroelasticity: Efficient modeling of strongly coupled, slow deformation processes in a multilayered half-space

Rongjiang Wang* and Hans-Joachim Kümpel‡

ABSTRACT

We present a fast, powerful numerical scheme to compute poroelastic solutions for excess pore pressure and displacements in a multilayered half-space. The solutions are based on the mirror-image technique and use an extension of Haskell's propagator method. They can be applied to assess in-situ formation parameters from the surface deformation field when fluids are injected into or extracted from a subsurface reservoir, or they can be used to simulate changes in pore-fluid pressure resulting from matrix displacements induced by an earthquake. The performance of the numerical scheme is tested through comparison with observations of the surface deformation as recorded by tiltmeters in the vicinity of an iteratively pumped well. Modeling of near-surface tilt data around a productive well is useful in constraining hydraulic diffusivity in the layered subsurface.

INTRODUCTION

Linear poroelasticity theory has become a useful tool for understanding and simulating physical rock-fluid interactions in situations where fluid-saturated rock is deformed. These comprise consolidation of porous media in response to loading (Biot, 1941; Zimmerman, 1991), occurrence of seismotectonically induced groundwater fluctuations (Roeloffs, 1988, 1996), propagation of seismic waves through porous media (e.g., Biot, 1962; Deresiewicz and Levy, 1967; Bourbié et al., 1987), land subsidence as a result of fluid extraction from subsurface reservoirs (Geertsma, 1973; Segall, 1985), production-induced strain near vicinity wells (Grasso, 1992; Kümpel, 1997), and other phenomena. Vasco et al. (2000) present a study from a geothermal test site and argue for using the surface deformation to image reservoir dynamics.

In this paper, we explore solutions for strongly coupled diffusion and deformation processes which can be induced by, for example, pump tests or earthquakes. Rice and Cleary (1976) and Cleary (1977) point out that analytical solutions for such poroelastic problems are only known for very elementary configurations, e.g., for a point source of anomalous pore pressure in the homogeneous full space. Many solutions valid in thermoelasticity, which has several aspects in common with poroelasticity, are inappropriate because they neglect the strong coupling between rock strain on the one hand and change in temperature or pore pressure on the other (Carslaw and Jaeger, 1959; Hart and John, 1986; H. Wang, 2000).

Booker and Carter (1986) present closed-form analytical solutions for the steady-state distribution of displacement, excess pore pressure, and stress around a point sink embedded in a homogeneous poroelastic half-space. The solutions are based on the mirror-image technique and are used by Lehmann (2001) to model near-surface tilt deformation induced by pumping groundwater from shallow depths. Segall (1985) and Vasco et al. (2000) show that the quasi-static problem in the poroelastic half-space can be solved by using the elastic Green's functions, provided the time-dependent spatial change in the fluid content is known or can be determined independently. More complex problems which also trace the transient behavior require superposition of elementary solutions or application of numerical techniques such as finite-difference or finite-element schemes (Booker and Small, 1977; Lewis and Schreffler, 1987). Alternative methods are helpful where analytical solutions are not available or where the use of such numerical procedures is laborious.

We present a fast, powerful numerical scheme to find transient and steady-state solutions in the homogeneous or layered poroelastic half-space in response to forcing through a point source such as fluid injection with sudden onset or matrix dislocation resulting from an earthquake. The approach can be used in various ways:

1) to predict near-surface inflation or consolidation around a well where fluid is injected or extracted;
2) to predict postseismic changes in the hydraulic heads of aquifers in an earthquake area;

Manuscript received by the Editor June 26, 2001; revised manuscript received August 1, 2002.
*GeoForschungsZentrum Potsdam (GFZ), Telegrafenberg, D-14473 Potsdam, Germany. E-mail: wang@gfz-potsdam.de.
‡Leibniz Institute for Applied Geosciences (GGA), Stilleweg 2, D-30655 Hannover, Germany. E-mail: kuempel@gga-hannover.de.

3) to simulate land subsidence resulting from fluid extraction from sedimentary basins; or
4) to image reservoir dynamics from the deformation field at the surface or, in principle, at arbitrary depth.

The numerical scheme is based on a combination of Haskell's propagator method (Thomson, 1950; Haskell, 1953) with poroelasticity theory. The loss-of-precision problem of the original Haskell algorithm is avoided using an orthonormalization extension as proposed by R. Wang (1999).

We demonstrate the effectiveness of the new approach by calculating pump-induced deformation in the vicinity of a well and compare the solutions with field data. Monitoring pump-induced strain near wells may be a promising technique to trace pore-pressure decline in an aquifer (Kümpel, 1989; Kümpel et al., 1996). Similarly, the near-surface deformation field can assess the propagation of fluids injected at depths (Vasco et al., 2000).

THE BOUNDARY VALUE PROBLEM

In poroelasticity the governing equations can be written as

$$(\lambda + 2\mu)\nabla(\nabla \cdot \mathbf{u}) - \mu\nabla \times (\nabla \times \mathbf{u}) - \alpha\nabla p = \mathbf{f}(\mathbf{x}, t), \tag{1}$$

$$Q^{-1}\frac{\partial p}{\partial t} + \alpha\frac{\partial}{\partial t}\nabla \cdot \mathbf{u} - \chi\nabla^2 p = q(\mathbf{x}, t), \tag{2}$$

where $\mathbf{u}$ is the displacement vector, p is excess pore pressure, λ and μ are Lamé coefficients, α is the dimensionless coefficient of effective stress (the change in pore pressure per unit change in bulk volume under drained conditions), Q^{-1} is the bulk compressibility introduced by Biot (1941), χ is Darcy conductivity, $\mathbf{f}$ is the body force per unit volume acting on the solid matrix, and q is the fluid volume injection rate; $\mathbf{f}$ and q are functions of spatial position $\mathbf{x}$ and time t. In practice, it is convenient to express λ, α, Q^{-1}, and χ in terms of the Skempton ratio B (the change in pore pressure per unit change in confining pressure under undrained conditions), the hydraulic diffusivity D, and the Poisson ratios ν and ν_u for drained and undrained conditions, respectively, whereby

$$\lambda = \frac{2\nu\mu}{1 - 2\nu}, \tag{3}$$

$$\alpha = \frac{3(\nu_u - \nu)}{(1 - 2\nu)(1 + \nu_u)B}, \tag{4}$$

$$Q^{-1} = \frac{9}{2}\frac{(1 - 2\nu_u)(\nu_u - \nu)}{(1 - 2\nu)(1 + \nu_u)^2\mu B^2}, \tag{5}$$

$$\chi = \frac{9}{2}\frac{(1 - \nu_u)(\nu_u - \nu)D}{(1 - \nu)(1 + \nu_u)^2\mu B^2}. \tag{6}$$

Overviews on poroelastic parameters are given by Kümpel (1991) and H. Wang (1993).

Equation (1) is derived from the equilibrium conditions,

$$\nabla \cdot \Gamma = \mathbf{f}(\mathbf{x}, t), \tag{7}$$

in combination with Hooke's generalized linear law adopted in poroelasticity,

$$\Gamma = (\lambda\nabla \cdot \mathbf{u} - \alpha p)\,\mathbf{I} + \mu[\nabla\mathbf{u} + (\nabla\mathbf{u})^T], \tag{8}$$

where Γ is the stress tensor and $\mathbf{I}$ is the unit tensor.

Equation (2) represents the conservation of water mass by applying Darcy's law to water flow in the pore space. In Biot's theory, the water contained in the pores is assumed to be incompressible. So the conservation of the water mass is equivalent with the conservation of the water volume. The terms $Q^{-1}\frac{\partial p}{\partial t}$ and $\alpha\frac{\partial}{\partial t}\nabla \cdot \mathbf{u}$ express the change in volumetric content of water per unit time caused by some increase in pore pressure and by dilatation of solid formation, respectively. Darcy's flux, i.e., the volume of water flowing per unit area and unit time, is

$$\mathbf{v} = -\chi\nabla p. \tag{9}$$

At an interior material interface, the continuity conditions are

$$\mathbf{u}\Big|_-^+ = \mathbf{0}, \tag{10}$$

$$\mathbf{e}_n \cdot \Gamma\Big|_-^+ = \mathbf{0}, \tag{11}$$

$$p\Big|_-^+ = 0, \tag{12}$$

$$\mathbf{e}_n \cdot \mathbf{v}\Big|_-^+ = 0, \tag{13}$$

where $\mathbf{e}_n$ is the interface normal. The symbol $|_-^+$ denotes the increment of the respective quantity from one side to the other side of an interface.

The conditions at the unconfined free surface are

$$\mathbf{e}_n \cdot \Gamma = \mathbf{0}, \tag{14}$$

$$p = 0. \tag{15}$$

ANALYTICAL SOLUTIONS FOR SOME SPECIAL CASES

Transient Green's functions for the homogeneous whole space

When dealing with injection or pump-induced deformation near a well, we are interested in Green's functions, which describe the response of a linear poroelastic diffusive solid to a point fluid volume injection source. Analytical solutions in closed form are only known for a few special cases. For sudden onset of a constant injection with rate q_o in the homogeneous whole space, we have

$$q(\mathbf{x}, t) = q_o\,\delta(\mathbf{x} - \mathbf{x}_s)\,H(t), \tag{16}$$

where $\mathbf{x}_s$ is the position of the point injection source, $\delta(\mathbf{x})$ is the 3D delta function, and $H(t)$ is the Heaviside function. According to Rudnicki (1986), in this case

$$\mathbf{u}(\mathbf{x}, t) = \frac{q_o(1 + \nu_u)B}{24\pi(1 - \nu_u)D}\,\frac{\mathbf{x} - \mathbf{x}_s}{R}\,F(\xi), \tag{17}$$

$$p(\mathbf{x}, t) = \frac{q_o}{4\pi\chi}\,\frac{1}{R}\mathrm{erfc}(\xi/2), \tag{18}$$

where $R = |\mathbf{x} - \mathbf{x}_s|$ is the distance to the point source, λ_u is the first Lamé modulus for undrained conditions, $\xi = R/\sqrt{Dt}$, and

$$F(\xi) = \operatorname{erfc}(\xi/2) + \frac{2}{\xi^2} g(\xi), \tag{19}$$

$$g(\xi) = \operatorname{erf}(\xi/2) - \frac{\xi}{\sqrt{\pi}} \exp\left(-\frac{\xi^2}{4}\right). \tag{20}$$

In the steady state ($t \to \infty$), $F(\xi) = \operatorname{erfc}(\xi/2) = 1$, i.e., the form of the whole-space solution becomes very simple. For convenience, when applying the solutions to situations around wells, we use the cylindrical coordinate system (z, r, θ), in which z is the symmetry axis, positive downward. The θ-coordinate is not used because of axial symmetry of the problem. If we place the point injection source at $z = d$ (corresponding to the injection depth from the surface), the steady-state whole-space solutions are expressed by

$$u_z(z, r) = u_o \frac{z - d}{R}, \tag{21}$$

$$u_r(z, r) = u_o \frac{r}{R}, \tag{22}$$

$$p(z, r) = p_o \frac{d}{R}, \tag{23}$$

where

$$R = \sqrt{(z - d)^2 + r^2}, \tag{24}$$

$$u_o = \frac{q_o(1 + \nu_u)B}{24\pi(1 - \nu_u)D} = \frac{\alpha d p_o}{2(\lambda + 2\mu)}, \tag{25}$$

$$p_o = \frac{q_o}{4\pi d \chi}. \tag{26}$$

Note that u_o and p_o express the absolute displacement and the pore pressure increase at distance $R = d$ from the injection source, respectively. For later use, we also give the surface stress components $\mathbf{e}_z \cdot \boldsymbol{\Gamma}$, computed from equation (8):

$$\Gamma_{zz}(z, r) = -2\mu u_o \left[\frac{(z - d)^2}{R^3} + \frac{1}{R}\right], \tag{27}$$

$$\Gamma_{zr}(z, r) = -2\mu u_o \frac{(z - d)r}{R^3}. \tag{28}$$

Steady-state Green's functions for the homogeneous half-space

Under free surface conditions given by equations (14) and (15), the Green's functions become more complicated. Booker and Carter (1986) present the complete set of steady-state half-space solutions in closed form using the mirror-image method. The same method is applied by Garbesi (1993) to assess pore-pressure distortions in response to periodic forcing. In this paper, the steady-state solutions are used as a reference for the numerical approach. We next outline the derivation of these solutions and indicate some minor typing errors in the original formulas of Booker and Carter (1986).

Assume that the half-space Green's functions take the form

$$u_z(z, r) = u_z^{(m)}(z, r) + u_z^{(c)}(z, r), \tag{29}$$

$$u_r(z, r) = u_r^{(m)}(z, r) + u_r^{(c)}(z, r), \tag{30}$$

$$p(z, r) = p^{(m)}(z, r) + p^{(c)}(z, r). \tag{31}$$

Here, the terms with superscript (m) express the result from the mirror-image method, i.e., that of the total field of the point injection source plus its negative image source (pumping) located at $z = -d$ in the upper half-space:

$$u_z^{(m)}(z, r) = u_o \left(\frac{z - d}{R} - \frac{z + d}{R'}\right), \tag{32}$$

$$u_r^{(m)}(z, r) = u_o \left(\frac{r}{R} - \frac{r}{R'}\right), \tag{33}$$

$$p^{(m)}(z, r) = p_o \left(\frac{d}{R} - \frac{d}{R'}\right), \tag{34}$$

where R' is the distance to the image source,

$$R' = \sqrt{(z + d)^2 + r^2}. \tag{35}$$

The corresponding stress components are

$$\Gamma_{zz}^{(m)}(z, r) = -2\mu u_o \left[\frac{2R^2 - r^2}{R^3} - \frac{2R'^2 - r^2}{R'^3}\right], \tag{36}$$

$$\Gamma_{zr}^{(m)}(z, r) = -2\mu u_o \left[\frac{(z - d)r}{R^3} - \frac{(z + d)r}{R'^3}\right]. \tag{37}$$

The terms with superscript (c) are necessary corrections to fully satisfy the conditions for a stress-free surface. Substituting equations (29)–(31) into equations (14) and (15), for the half-space the correction terms are determined by the boundary-value problem

$$(\lambda + 2\mu)\nabla(\nabla \cdot \mathbf{u}^{(c)}) - \mu \nabla \times (\nabla \times \mathbf{u}^{(c)}) = \alpha \nabla p^{(c)}, \tag{38}$$

$$\nabla^2 p^{(c)} = 0, \tag{39}$$

for $(z > 0)$. At the surface $(z = 0)$,

$$p^{(c)} = -p^{(m)} = 0, \tag{40}$$

$$\Gamma_{zz}^{(c)} = -\Gamma_{zz}^{(m)} = 0, \tag{41}$$

$$\Gamma_{zr}^{(c)} = -\Gamma_{zr}^{(m)} = -4\mu u_o d \frac{r}{\sqrt{\left(d^2 + r^2\right)^3}}. \tag{42}$$

It is obvious that the correction for the excess pore pressure vanishes:

$$p^{(c)}(z, r) = 0. \tag{43}$$

Thus, in steady state the problem is purely elastic. Its can be solved using the Hankel transform (see, e.g., Farrell, 1972).

The results are given by

$$u_z^{(c)}(z,r) = -2u_o\, d\left[\frac{z(z+d)}{R'^3} + \frac{1-2\nu}{R'}\right], \tag{44}$$

$$u_r^{(c)}(z,r) = -2u_o d\left[\frac{zr}{R'^3} + \frac{2(1-\nu)}{r}\left(\frac{z+d}{R'} - 1\right)\right]. \tag{45}$$

The closed analytical expressions for the steady-state half-space solution are

$$u_z(z,r) = u_o\left[\frac{z-d}{R} - \frac{z+d}{R'} - \frac{2(1-2\nu)d}{R'} - \frac{2dz(z+d)}{R'^3}\right], \tag{46}$$

$$u_r(z,r) = u_o\left[\frac{r}{R} - \frac{r}{R'} - \frac{2dzr}{R'^3} - \frac{4(1-\nu)d}{r}\left(\frac{z+d}{R'} - 1\right)\right], \tag{47}$$

$$p(z,r) = p_o\left(\frac{d}{R} - \frac{d}{R'}\right), \quad (z \geq 0). \tag{48}$$

The two displacement components noted in equations (46) and (47) are slightly different from the corresponding formulas presented by Booker and Carter (1986) [see their equations (28) and (37)]. First, our coefficient u_o differs from their corresponding coefficient $A/2$ by the factor α because those authors have implicitly set $\alpha = 1$ in the poroelastic extension of Hooke's law. Second, the term $[(z-d)/R] - [(z+d)/R']$ in equation (46) is misspelt in Booker and Carter (1986) to $z/R_b - z/R_a$, which corresponds to $z/R - z/R'$ in the present notation.

Experimental verification of these solutions would require monitoring ground displacements and pore-pressure changes in controlled injection or pump tests. In practice, the surface displacement induced by a local pump test is below the 1-mm level and cannot be observed by leveling or global positioning system (GPS) techniques. Instead, tilt measurements of resolution 0.1 microradian (equivalent to the deflection of a 1-m-long vertical plumb line by 0.1 μm at its tip) or better should be able to check equations (46)–(48) under field conditions. A borehole tiltmeter measures the vertical tilt, which is defined by

$$\Delta\gamma = -\frac{\partial u_r}{\partial z}. \tag{49}$$

In this definition, a positive value of $\Delta\gamma$ means that the upper end of a tiltmeter body moves away from a pumped well. For the homogeneous whole-space model, the steady-state solution for the tilt is

$$\Delta\gamma(z,r) = u_o r\frac{z-d}{R^3}, \tag{50}$$

whereas for the homogeneous half-space model we find

$$\Delta\gamma(z,r) = u_o r\left[\frac{z-d}{R^3} - \frac{z+(4\nu-5)d}{R'^3} - \frac{6dz(z+d)}{R'^5}\right]. (z \geq 0). \tag{51}$$

Figure 1 shows both solutions for tilt at horizontal distance $r = d/\sqrt{2} \sim 0.7d$. At this distance, surface tilt for both the whole-space and half-space models is largest. As expected, whole-space and half-space solutions agree well for large depths. At the surface, however, the difference between the two solutions reaches a maximum. In particular,

$$\left.\frac{\Delta\gamma(\text{half-space})}{\Delta\gamma(\text{whole-space})}\right|_{z=0} = -4(1-\nu), \tag{52}$$

i.e., the half-space theory predicts an inverse and about three times larger surface tilt (for ν close to 0.25) than the whole-space model. This result is verified by observations of Kümpel (1989), Kümpel et al. (1996), and Lehmann (2001), who find that the whole-space theory can only explain pump-induced tilt data sensed at depths around or below the productive well screen. For tiltmeters installed at more shallow depth, the recorded tilt data exhibit opposite sign; that is, the upper end of a tiltmeter body tilts toward a pumped well—not the lower end, as predicted in the whole-space model. The cause is the free surface effect as presented above, i.e., dominance of rotational movements over shear strain. Figure 1 also shows how strongly the correction terms contribute to the half-space tilt solution.

NUMERICAL SOLUTIONS FOR A MULTILAYERED HALF-SPACE

Laplace-Hankel transform in poroelasticity

A multilayered half-space consists of an arbitrary but finite number of individual, homogeneous, horizontal layers with a stress-free surface on top and the deepest layer extending to infinite depth. Solving a problem in a multilayered half-space

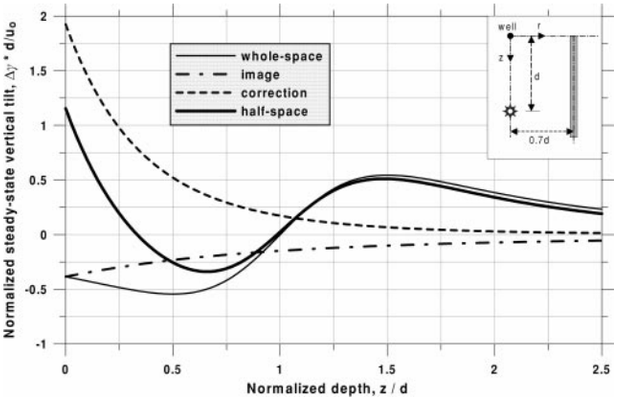

FIG. 1. Analytical poroelastic solutions ($\nu = 0.25$) for steady-state vertical tilt induced by constant-rate fluid injection at point $z = d, r = 0$ along a vertical profile at a fixed horizontal distance $r = d/\sqrt{2} \sim 0.7d$ (see inset). Positive tilt indicates the upper end of the tiltmeter body moves toward the well, relative to its lower end. In the half-space at the surface ($z = 0$), the upper end of the tiltmeter body rotates outward in response to fluid injection at depth, unlike the predictions of the whole-space model (at respective vertical distance). The half-space solution is a sum of the whole-space solution, the image solution, and the correction term.

situation requires applying of numerical methods. In the following, we adopt the well-known Haskell propagator method (Thomson, 1950; Haskell, 1953), which has been widely used for calculating values such as seismic wave propagation in layered poroelastic media (see, for example, Deresiewicz and Levy, 1967; Allard et al., 1986). In this method, the Laplace-Hankel transform is applied to the solution vectors.

The Laplace transform is achieved when the partial derivative $\frac{\partial}{\partial t}$ in the equation of motion is replaced by the Laplace parameter s. The Hankel transform is expressed by

$$\mathbf{u}(z,r,\theta,s) = \sum_m \int_0^\infty [U_m(z,s)\,\mathbf{Z}_k^m(r,\theta) + V_m(z,s)\,\mathbf{R}_k^m(r,\theta) + W_m(z,s)\,\mathbf{T}_k^m(r,\theta)]\,k\,dk, \quad (53)$$

$$\mathbf{e}_z \cdot \boldsymbol{\Gamma}(z,r,\theta,s) = \sum_m \int_0^\infty [E_m(z,s)\,\mathbf{Z}_k^m(r,\theta) + F_m(z,s)\,\mathbf{R}_k^m(r,\theta) + G_m(z,s)\,\mathbf{T}_k^m(r,\theta)]\,k\,dk, \quad (54)$$

$$p(z,r,\theta,s) = \sum_m \int_0^\infty P_m(z,s)\,Y_k^m(r,\theta)\,k\,dk, \quad (55)$$

$$v_z(z,r,\theta,s) = \sum_m \int_0^\infty Q_m(z,s)\,Y_k^m(r,\theta)\,k\,dk, \quad (56)$$

where

$$Y_k^m(r,\theta) = J_m(kr)\begin{pmatrix}\cos m\theta \\ \sin m\theta\end{pmatrix}, \qquad m = 0,1,2,\ldots \quad (57)$$

are the cylindrical surface harmonics and

$$\mathbf{Z}_k^m(r,\theta) = \mathbf{e}_z Y_k^m(r,\theta), \quad (58)$$

$$\mathbf{R}_k^m(r,\theta) = \mathbf{e}_r \frac{1}{k}\frac{\partial}{\partial r} Y_k^m(r,\theta) + \mathbf{e}_\theta \frac{1}{kr}\frac{\partial}{\partial \theta} Y_k^m(r,\theta), \quad (59)$$

$$\mathbf{T}_k^m(r,\theta) = \mathbf{e}_r \frac{1}{kr}\frac{\partial}{\partial \theta} Y_k^m(r,\theta) - \mathbf{e}_\theta \frac{1}{k}\frac{\partial}{\partial r} Y_k^m(r,\theta) \quad (60)$$

are the corresponding surface vector harmonics (see, e.g., Aki and Richards, 1980). For a point fluid injection, only the harmonics of degree $m = 0$ are needed; for a single force, $m = 0, 1$; for a double couple source, $m = 0, 1, 2$; and so on.

We first consider a homogeneous medium without any source. Application of the Laplace-Hankel transform to equations (1) and (2) yields two systems of ordinary differential equations. The first system governs the coupled matrix displacement and the pore pressure field, that is,

$$\frac{d}{dz}\mathbf{y}_m = \mathbf{A}\cdot\mathbf{y}_m, \quad (61)$$

where

$$\mathbf{y}_m = (U_m, E_m, V_m, F_m, P_m, Q_m)^T \quad (62)$$

expresses a generalized 6D displacement vector called the poloidal field and where

$$\mathbf{A} = \begin{pmatrix} 0 & \frac{1}{\zeta} & \frac{\lambda k}{\zeta} & 0 & \frac{\alpha}{\zeta} & 0 \\ 0 & 0 & 0 & k & 0 & 0 \\ -k & 0 & 0 & \frac{1}{\mu} & 0 & 0 \\ 0 & -\frac{\lambda k}{\zeta} & \frac{4\mu\eta k^2}{\zeta} & 0 & \frac{2\alpha\mu k}{\zeta} & 0 \\ 0 & 0 & 0 & 0 & 0 & -\frac{1}{\chi} \\ 0 & -\frac{\alpha s}{\zeta} & \frac{2\mu\alpha k s}{\zeta} & 0 & -\chi k_p^2 & 0 \end{pmatrix}, \quad (63)$$

with

$$\zeta = \lambda + 2\mu, \quad (64)$$

$$\zeta_1 = \zeta + \alpha^2 Q, \quad (65)$$

$$\eta = \lambda + \mu, \quad (66)$$

$$k_p = \sqrt{k^2 + \frac{\zeta_1 s}{\chi\zeta Q}}. \quad (67)$$

The second system is two dimensional and governs matrix displacements decoupled from the pore pressure, namely,

$$\frac{d}{dz}\mathbf{x}_m = \mathbf{B}\cdot\mathbf{x}_m, \quad (68)$$

where

$$\mathbf{x}_m = (W_m, G_m)^T \quad (69)$$

is called the toroidal field and where

$$\mathbf{B} = \begin{pmatrix} 0 & \frac{1}{\mu} \\ -\mu k^2 & 0 \end{pmatrix}. \quad (70)$$

The solution of the toroidal system is well known in elasticity theory and is not interesting for the present work.

The boundary conditions [equations (10)–(13)] at a material interface are converted to the continuity conditions of the generalized displacement vector,

$$\mathbf{y}_m\big|_-^+ = \mathbf{0}. \quad (71)$$

The source conditions can be expressed by a step function of the vector $\mathbf{y}_m$ at the source plane, $z = z_s$. When we are interested in the point injection source given by equation (16), the Laplace-Hankel transform of the source function is

$$q_o\delta(\mathbf{x}-\mathbf{x}_s)\,H(t) \;\Rightarrow\; \frac{q_o}{2\pi s}\,\delta(z-z_s), \quad (m=0).$$

The source conditions are then expressed as

$$\mathbf{y}_m\big|_-^+ = \mathbf{y}_m(z_s^+) - \mathbf{y}_m(z_s^-) = \Delta\mathbf{y}_m(z_s) = \left(0,0,0,0,0,\frac{q_o}{2\pi s}\right)^T, \quad (m=0). \quad (72)$$

Other source conditions concerning single-force or double-couple dislocations can be handled as indicated by Kennett (1983).

In the following, the index m of the vector $\mathbf{y}_m$ is omitted for simplicity without leading to any confusion.

Fundamental poroelastic solutions

Suppose equation (61) has solutions in the form

$$\mathbf{y}(z) = \mathbf{y}^{(\nu)}\, e^{\nu z}, \tag{73}$$

where

$$\mathbf{y}^{(\nu)} = \boldsymbol{\beta} = (\beta_1, \ldots, \beta_6)^T \tag{74}$$

is a constant vector. Then determination of $\boldsymbol{\beta}$ requires solving the eigenvalue problem,

$$(\mathbf{A} - \nu\mathbf{I})\, \mathbf{y}^{(\nu)} \;=\; \mathbf{0}. \tag{75}$$

We obtain the complete set of six eigenvalues using the Mathematica symbolic manipulation software (Wolfram, 1988). Accordingly,

$$\nu = \{\nu_1, \ldots, \nu_6\} = \{k, -k, k, -k, k_p, -k_p\}. \tag{76}$$

Since both $+k$ and $-k$ are second-order eigenvalues their corresponding eigenvectors $\mathbf{y}^{(\nu)}$ should be noted as linear functions instead of constants, i.e.,

$$\mathbf{y}^{(\nu)} = (\boldsymbol{\beta} + \nu z\, \boldsymbol{\gamma}), \tag{77}$$

with

$$\boldsymbol{\gamma} \;=\; (\gamma_1, \ldots, \gamma_6)^T \tag{78}$$

being another constant vector. Finally, the eigenvalue problem is extended to a 12×12 matrix system,

$$\begin{pmatrix} \mathbf{A} - \nu\mathbf{I} & -\mathbf{A} \\ \mathbf{0} & \mathbf{A} - \nu\mathbf{I} \end{pmatrix} \begin{pmatrix} \boldsymbol{\beta} \\ \boldsymbol{\gamma} \end{pmatrix} = \mathbf{0}, \tag{79}$$

which can also be solved by Mathematica©.

The extended Haskell's propagator algorithm

For any homogeneous layer in one dimension, the displacement vector at the depth $z = h$ of a poroelastic disturbance is related to its value at the top ($z = 0$) by

$$\mathbf{y}(h) = \mathbf{H}(h) \cdot \mathbf{y}(0), \tag{80}$$

$$\mathbf{H}(h) = \mathbf{L}(h) \cdot \mathbf{E}(h) \cdot \mathbf{L}^{-1}(0), \tag{81}$$

where $\mathbf{H}$ is the generalized 6×6 Haskell's propagator and $\mathbf{L}$ is the 6×6 layer matrix, the six columns of which consist of the six fundamental solution vectors $\mathbf{y}^{(\nu_i)}$ ($i = 1, \ldots, 6$), i.e.,

$$\mathbf{L}(z) \;=\; (\mathbf{y}^{(\nu_1)}(z), \ldots, \mathbf{y}^{(\nu_6)}(z)). \tag{82}$$

The elements of the poroelastic layer matrix $\mathbf{L}$ and its inverse $\mathbf{L}^{-1}$ are given in Appendix A; $\mathbf{E}$ is the 6×6 diagonal matrix:

$$\mathbf{E}(z) = dia(e^{kz}, e^{-kz}, e^{kz}, e^{-kz}, e^{k_p z}, e^{-k_p z}). \tag{83}$$

Note that the first, third, and fifth column vectors of $\mathbf{L}(z)$ represent upgoing waves with different characteristic amplitude factors e^{kz}, $(kz)\, e^{kz}$, and $e^{k_p z}$; the second, fourth, and sixth column vectors are the corresponding downgoing waves with amplitude factors e^{-kz}, $(kz)\, e^{-kz}$, and $e^{-k_p z}$, respectively.

Inside a poroelastically uniform layer, the depth-dependent solution is given by

$$\mathbf{y}(z) \;=\; \mathbf{L}(z) \cdot \mathbf{E}(z) \cdot \mathbf{c}, \tag{84}$$

where $\mathbf{c}$ is a constant coefficient vector,

$$\mathbf{c} \;=\; (A^+, A^-, B^+, B^-, C^+, C^-)^T. \tag{85}$$

At layer interfaces, the continuity conditions progress successively, thereby relating the poroelastic solution vector from depth to depth. In Haskell's propagator algorithm, a set of fundamental solution vectors satisfying the surface conditions is first computed via the matrix propagation. The desired solution is then obtained by a linear superposition of the fundamental solutions, the weighting coefficients of which are finally determined by the source conditions. A program-ready flowchart for the Haskell propagator algorithm in this context is given in Appendix B to demonstrate its use.

Computational results using the original Haskell's propagator algorithm (as stated above) exhibit numerical instabilities. The cause is the known loss-of-precision problem which arises when differently evanescent solution vectors are numerically coupled. A number of publications have attempted to solve this difficulty (Knopoff, 1964; Dunkin, 1965; Jovanovich et al., 1974; Kennett, 1983; Chin et al., 1984; R. Wang, 1999). We use the orthonormalization extension proposed by R. Wang (1999), outlined in Appendix C.

Having found the solutions in the Laplace-Hankel domain, we use the Bessel integrations in equations (53)–(56) and the inverse Laplace transform to yield the desired solutions in the space–time domain.

TEST RESULTS

For a first demonstration of the algorithm, we present the transient ground tilt signal induced by a point fluid injection source in a homogeneous poroelastic half-space. The parameter values adopted for the model are $\mu = 0.4$ GPa, $\nu = 0.2$, $\nu_u = 0.4$, $B = 0.75$, and $D = 1.0$ m^2/s, which could represent an unconsolidated sandy aquifer. With reference to a field example presented below, the point source is placed at depth $d = 60$ m and starts with sudden onset at time $t = 0$ and constant injection rate $q_o = 32$ m^3/hour (0.009 m^3/s).

We compute the induced changes in excess pore pressure and in vertical tilt at a fixed horizontal distance $r = 40$ m. The results for depths $z = 5$, 15, 45, and 75 m are shown in Figure 2, together with analytical solutions for the homogeneous whole-space. It is obvious from Figure 2, that pore pressure needs a longer time than the vertical tilt to reach steady state, but convergence is accelerated in the half-space situation, i.e., when the free surface effect is taken into account. Moreover, at shallow depths the half-space results initially show a weak pore pressure decline. The phenomenon has often been observed with pump tests in layered formations. It has occasionally been described as the Noordbergum effect in the literature (Verruijt, 1969; Maruyama, 1994; Kim and Parizek, 1997), referring to a location in The Netherlands where the effect has been noted. The Noordbergum effect is explained by coupling in bounded poroelastic media. Whereas the elastic interaction is instantaneous, the transport of pore fluid to equilibrate excess pore pressure follows the diffusion law and is therefore delayed. Accordingly, at some distance from the injection point, the solid

matrix initially responds elastically rather than poroelastically to the onset of fluid injection. Using the solutions for internal deformation in elastic media of Okada (1992), we can see that the elastic volume strain near the surface ($z \ll d$) is positive (dilatation) for $r < \sqrt{2}\,d$ and negative (compression) for $r > \sqrt{2}\,d$. The volume dilatation at the observation distance ($r = \frac{2}{3}d < \sqrt{2}\,d$) thus results in a short-term drop of the pore pressure, that is, the Noordbergum effect appears. Differences in pore pressure between the half-space and whole-space solutions decrease with depth.

This also holds for the ground tilt. However, at shallow depths, whole-space and half-space solutions yield opposite signs for the tilt response: In the whole space, shear strains shift the part of the tiltmeter body nearest to the injection source further away than the more distant end of the instrument; closer to the free surface, dominance of rotational movements forces the upper end of the tiltmeter to displace more than its lower end. This result confirms the steady-state solutions presented in Figure 1. Note that the transient signals computed for the poroelastic half-space also predict occurrence of the Noordbergum effect in the tilt data (for depths around $z = 15$ m; see Figure 2).

To test the accuracy of our numerical approach, we computed the whole-space transient solutions with the propagator program and compared them with the exact analytical results. The numerical errors turned out to be smaller than the thickness of the lines in Figure 2.

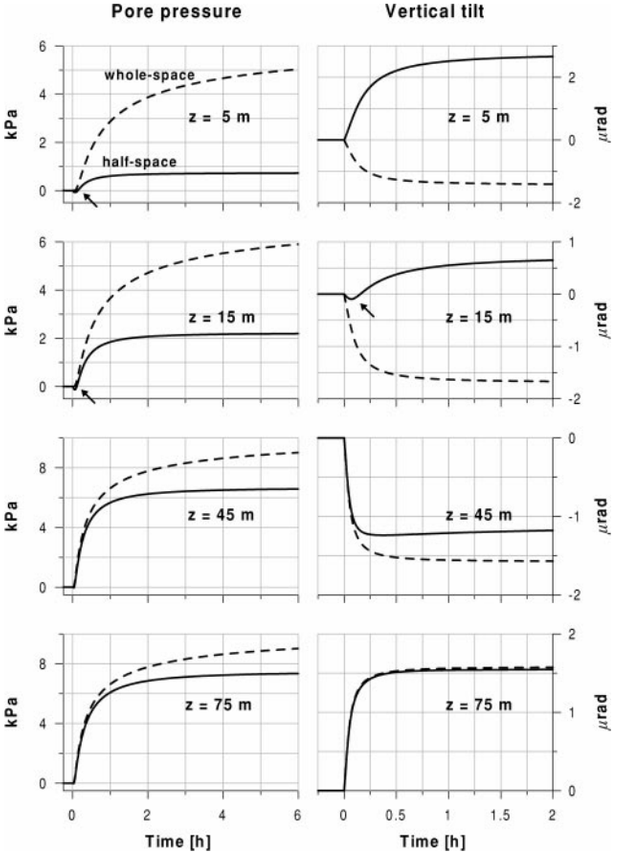

FIG. 2. Transient excess pore pressure and vertical ground tilt at four different depths induced by fluid injection through a point source with sudden onset and constant injection rate at depth $d = 60$ m in a homogeneous poroelastic medium at fixed horizontal distance $r = 40$ m. Values of poroelastic parameters are as for a sandy aquifer with hydraulic diffusivity $D = 1.0$ m^2/s; injection starts at time zero at $q_0 = 32$ m^3/h. Solid lines show the results of the half-space calculated using the numerical propagator method; broken lines display predictions for the whole-space situation as obtained by analytical expressions. Note different scales on the amplitude and time axes and the occurrence of the Noordbergum effect, denoted by the arrows.

APPLICATION TO A FIELD CASE

To verify the solutions for the layered half-space, we did some computations and compared the results with field data obtained at a test site in the small town of Nagycenk near Sopron in western Hungary. In the vicinity of a groundwater production well here, two borehole tiltmeters were installed at four different positions to monitor the surface deformation response to pumping (Figure 3). The total depth of the well is 78.5 m. Groundwater is produced from two aquifers—namely, from 56.2 to 60.7 m and from 65.7 to 74.0 m depth below surface (Kümpel et al., 1996). On average, the pump is active 2 to 3 times a day, producing at a rate of about 32 m^3/hour for several hours. From the drillers' notes, we surmised the subsurface consists of layered unconsolidated sediments, mainly loam with sands and sandy loam, with occasional intercalations of mixed size gravels (Gyula Mentes, personal communication, 1995). The productive aquifers consist of coarse- and medium-size-gravel. The mean groundwater table is 3.3 m below surface.

During the test phase, the borehole tiltmeters were installed at distances 7.7, 6.9, 22.9, and 64 m at positions 1 to 4 from the well (Figure 3). Biaxial bubble sensors were used for this study (Agnew, 1986) with a resolution of 0.1 microradian (Applied Geomechanics, Inc., 1991, User's Manual B-91-1004, Model 722 Borehole Tiltmeter). From mid-1995 until mid-1997, one tiltmeter was permanently installed at 4.3 m depth at position 1; the other one was temporarily monitoring at depths of 4.3, 2.8, and 3.8 m at position 2, 3, or 4. Some early data of this study are presented by Kümpel et al. (1996). Lehmann (2001) uses the tilt recordings for a more detailed analysis with

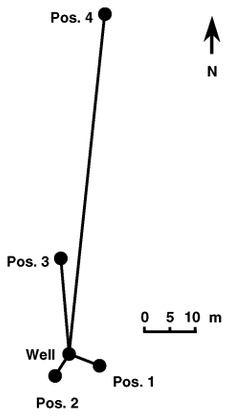

FIG. 3. Site map of the test site Nagycenk, Hungary, with positions 1 to 4 of shallow borehole tiltmeters relative to a groundwater production well. Topography is negligible in the area.

interpretation of the steady-state response for the homogeneous half-space.

For computing the transient layered half-space solution, poroelastic parameter values for the various layers were adopted (Table 1). Soil samples for laboratory tests were not available, so values are rough guesses. The unsaturated zone was disregarded. The Poisson ratios ν, ν_u for drained and undrained conditions and the Skempton ratio B were taken as uniform over the whole depth range. A slight increase of the shear modulus with depth was adopted to account for some loading-induced consolidation. Accordingly, the layering is mainly reflected in different hydraulic diffusivities D_A, roughly representing the drillers' description of the type of sediments.

Figure 4 shows one week of data of the observed pump-induced tilt signals at positions 1 and 3, together with the forcing function, i.e., the pump cycles. The tilt plotted is the inclination of the earth's surface in the radial direction away from the producing well. Positive signals indicate outward tilting, as if the wellhead would rise; negative signals mean inward tilting (subsidence of the wellhead). There is general agreement between the observed tilt signals and the causative pump cycles. The tilt amplitudes are well above the noise level, which is about 0.5 microradian for this site. At first look, it may be surprising that the amplitudes at the more distant position 3 are nearly twice as large as at position 1. This is a consequence of the fact that the producing section is much deeper than position 1 is distant from the well, whereas position 3 is at a distance more similar to the depth of the productive well screens. For the homogeneous half-space, strongest surface inclinations would in fact be expected at the distance where a cone of opening angle $2 \times 35.3^{\circ}$ toward the surface, centered with its tip in the productive depth, meets the surface (Lehmann, 2001), that is, 40–52 m from the well for the configuration here.

Tilt in tangential directions to the well should be zero in isotropic layered media. For the Nagycenk test site, tangential components of the pump-induced tilt at positions 1 and 3 were observed to be 19% and 6% of the strength of the radial components, respectively, indicating some anisotropy or lateral inhomogeneity is present.

The pumping that was ongoing for about 16 hours on the fifth day of this week in 1996 was exceptional. It helped discriminate between various subsurface models (the results of three are displayed in Figure 4). First, solutions were computed with model parameters as in Table 1, taking the first-guess values D_A as hydraulic diffusivities (model A). The calculated tilt amplitudes seem to match the observations at positions 1 and 3 rather well, but saturation (steady-state tilt) is delayed in the simulated signals, which is particularly obvious for the longlasting pump cycle. For this event the calculated tilt amplitude tends to attain a much higher steady-state response than was observed. Drift rates in the calculated tilt signals at the beginning of this week are transient because of the assumption of equilibrium pore pressure and zero strain as initial conditions. This effect is of no further importance here.

Convergence should occur earlier with higher hydraulic diffusivities, so a second set of solutions was computed taking five times higher values for the two productive zones (D_B in Table 1; model B). The tilt response to the pump cycles was faster, yet the amplitudes became too small (Figure 4). In a third run, diffusivities D_C were adopted with uniformly high values in the unproductive zones and just two times higher values for the two aquifers (model C). As a result, shape and amplitude of the calculated signals fit quite well with the observations at both positions. We have not been attempted to find the perfect fit because information about the true structure of

Table 1. Parameter values for poroelastic layers at test site in Nagycenk, Hungary. Uniform values 0.2, 0.4, and 0.75 were adopted for Poisson's ratios ν, ν_u and the Skempton ratio B. The values D_A, D_B, D_C are hydraulic diffusivities used in model runs A, B, C (underlined if changed with respect to previous model run).

Depth (m)	μ (GPa)	D_A (m^2/s)	D_B (m^2/s)	D_C (m^2/s)
0–6	0.20	0.50	0.50	0.50
6–26	0.30	0.01	0.01	0.25
26–32	0.30	0.07	0.07	0.25
32–55	0.40	0.01	0.01	0.25
55–62	0.40	1.00	5.00	1.00
62–64	0.40	0.01	0.01	0.25
64–74	0.40	1.00	5.00	1.00
74–∞	0.40	0.01	0.01	0.25

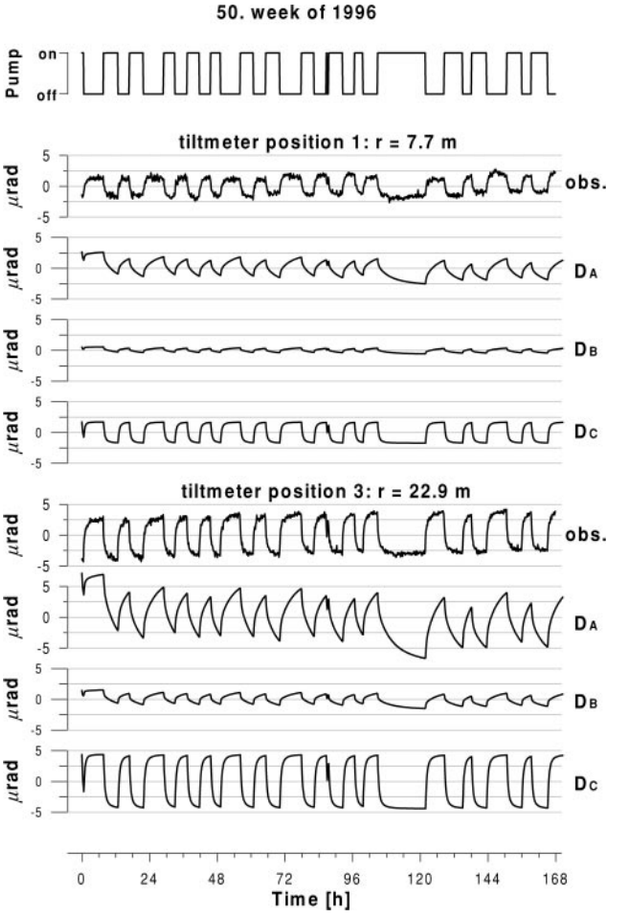

FIG. 4. Observed and computed ground tilt induced by pump activities in week 50 of 1996 at Nagycenk, Hungary. Water is simultaneously pumped from aquifers at depths of 56 to 61 m and 66 to 74 m. Tiltmeters were installed in shallow boreholes ($z < 4$ m) at distances $r = 7.7$ and 22.9 m, respectively. Computational results were obtained for the same horizontal distances with uniform pumping in both aquifers and parameters as listed in Table 1.

the subsurface is lacking. Also, some mismatch can easily be attributed to deviations of the field situation from the ideally layered 1D model. Nevertheless, the calculations demonstrate that there is considerable sensitivity of the overall solution to a suitable set of hydraulic diffusivities.

Figures 5 and 6 show tilt data of two different weeks, during which the second instrument was placed at position 2 or 4, respectively. Computational results are presented for model C data only. There is good agreement between the calculated data and the observations, so model C can be regarded as a good approach to the poroelastic layering at this site. At 64 m distance from the well (position 4), tilt amplitudes are two to three times higher than within a 10-m radius of the well. Tangential components of the tilt at positions 2 and 4 make up 26% and 6% of the radial components, respectively.

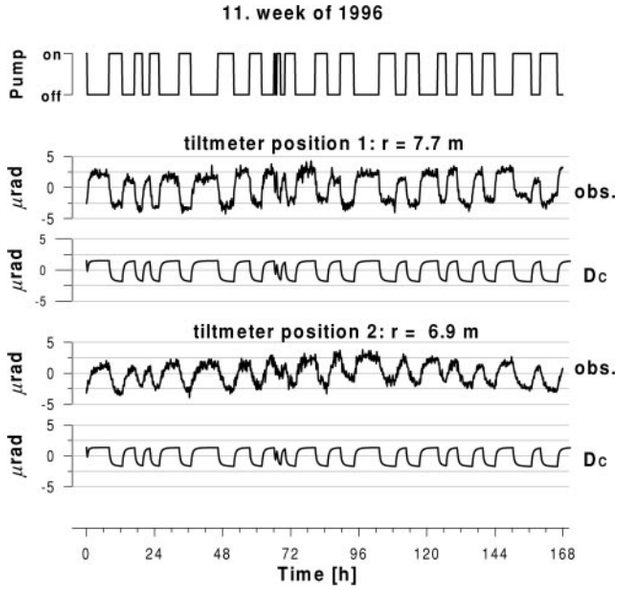

FIG. 5. Same as Figure 4, but data from week 11 of 1996 for tiltmeters at horizontal distances $r = 7.7$ and 6.9 m, respectively, and calculated tilts for hydraulic diffusivities D_C only.

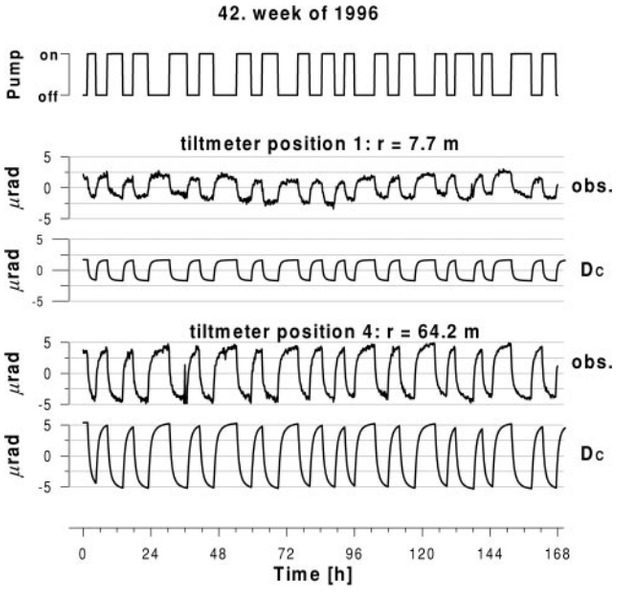

FIG. 6. Same as Figure 4, but data from week 42 of 1996 for tiltmeters at horizontal distances $r = 7.7$ and 64.2 m, respectively, and calculated tilts for hydraulic diffusivities D_C only.

DISCUSSION AND CONCLUSIONS

Surface deformation may provide useful constraints on the state of a reservoir that is being tested, under production, chosen to store critical liquid wastes injected from the surface, or used to produce geothermal energy. Vasco et al. (2000) detail the potential of this newly emerging technique to image fluid reservoir dynamics in the subsurface. In many cases, the principles of poroelasticity can be applied to model the relevant physical rock–fluid interactions involved. Since reservoir fluids are only accessible through wells and vertical boreholes are typically used to force fluids into a formation, axisymmetric solutions are of particular interest. Wide application of modeling techniques is, however, hampered by the strong coupling between pore pressure and matrix displacements, requiring the use of elaborate numerical schemes except for very elementary cases.

The analytical solutions presented by Booker and Carter (1986) are valid for steady-state situations where fluids are injected into or withdrawn from a reservoir, provided that the homogeneous half-space is a reasonable approach. At shallow depths, the solutions clearly deviate from the whole-space situation in that rotational movements dominate over displacements associated with shear strains, leading, e.g., to sign inversion of tilt signals in certain areas.

The newly introduced numerical scheme based on Haskell's propagator method can be applied to compute time-dependent solutions in configurations where a half-space consisting of an arbitrary number of laterally extended layers with individual poroelastic characteristics is the more suitable approach. Our algorithm is a powerful tool for various reasons:

1) it is faster than traditional numerical schemes when respective discretization of the object region is chosen and solutions are sought for single locations only;
2) a problem is easily formulated, as only a set of five poroelastic parameters per layer and the layer thicknesses need to be specified;
3) it is highly flexible, as forcing functions of point injection, single force, double couple source, etc., may be readily incorporated; and
4) the so-called loss-of-precision problem is overcome by orthonormalization.

Model calculations simulating the homogeneous half-space case confirm the steady-state solutions for pore pressure and tilt signals obtained through the aforementioned analytical expressions. Moreover, they show that the Noordbergum effect is reproduced in both pore pressure distortion and tilt deformation.

Haskell's propagator method is most useful in cases where near-surface deformation data are available from the surroundings of injection or pumping wells. Tiltmeters of resolution 0.1 microradian appear to be particularly adept at detecting small-amplitude signals, as from well testing in the context of normal groundwater production. We estimate that amplitudes of 1 microradian are seen up to distances of 100 m when the pumping

source is at depths of several tens of meters and production rate is of order 50 m^3/hour. The field data from the Nagycenk test site may be regarded as a typical example for the use of this algorithm. Instruments of higher resolution are required when the source depth is greater than a few hundred meters, depending also on the poroelastic compressibility of the subsurface medium. Techniques such as repeated leveling, GPS, or differential synthetic aperture radar (DSAR) become promising only when large amounts of fluids are injected or produced. Their detection level for vertical surface displacements is on the order of 1 mm, which corresponds to a surface tilt of 1 microradian if the spatial wavelength is on the order of 1 km.

The field data from Nagycenk demonstrate the effectiveness of the new approach in constraining the effective hydraulic diffusivity at depth. Occurrence of nonzero tangential tilt signals has, however, also shown that anisotropy may be a significant limiting factor for application of axisymmetric solution, in general. Nonradial pump-induced tilt has been reported from other locations as well (Kümpel, 1982; Weise, 1992; Lehmann, 2001). Seen from the other side, axisymmetric solutions help identify the isotropic part of the response to fluid withdrawal (or injection) and help isolate the anisotropic part. The latter may, in fact, contain valuable information on directional permeability or lateral heterogeneities within the reservoir. Ultimately, monitoring the surface deformation field in areas where fluid is extracted from or injected into subsurface layers may become an eminent tool in exploration geophysics to delineate irregularities in consolidation or inflation of rock matrix as a result of forced fluid flow at depth.

ACKNOWLEDGMENTS

We thank Gyula Mentes and Klaus Lehmann for providing tilt data from the test site at Nagycenk, Hungary. The site was operated as part of a German-Hungarian cooperation between the Geological Institute of Bonn University and the Geodetic-Geophysical Research Institute of the Hungarian Academy of Sciences, Sopron. We are grateful to one reviewer for drawing our attention to relevant prior work in this field. Three other reviewers gave helpful comments.

REFERENCES

Agnew, D. C., 1986, Strainmeters and tiltmeters: Rev. Geophys., **24**, 579–624.
Aki, K., and Richards, P. G., 1980, Quantitative seismology—Theory and methods: W. H. Freeman & Co.
Allard, J.-F., Bourdier, R., and Depollier, C., 1986, Biot waves in layered media: J. Appl. Phys., **60**, 1926–1929.
Biot, M. A., 1941, General theory of three-dimensional consolidation: J. Appl. Phys., **12**, 155–164.
———1962, Generalized theory of acoustic propagation in porous dissipative media: J. Acoust. Soc. Am., **34**, 1254–1264.
Booker, J. R., and Carter, J. P., 1986, Analysis of a point sink embedded in a porous elastic half space: Internat. J. Numer. Anal. Meth. Geomech., **10**, 137–150.
Booker, J. R., and Small, J. C., 1977, Finite element analysis of primary and secondary consolidation: Internat. J. Sol. Struct., **13**, 137–149.
Bourbié, T., Coussy, O., and Zinszner, B., 1987, Acoustics of porous media: Editions Technip.
Carslaw, H. S., and Jaeger, J. C., 1959, Conduction of heat in solids: Oxford Univ. Press.
Chin, R. C. Y., Hedstrom, G. W., and Thigpen, L., 1984, Matrix methods in synthetic seismograms: Geophys. J. Roy. Astr. Soc., **77**, 483–502.
Cleary, M. P., 1977, Fundamental solutions for a fluid saturated porous solid: Internat. J. Sol. Struct., **13**, 785–806.
Deresiewicz, H., and Levy, A., 1967, The effect of boundaries on wave propagation in a liquid-filled porous solid: X—Transmission through a stratified medium: Bull. Seis. Soc. Am., **57**, No. 3, 381–391.
Dunkin, J. W., 1965, Computation of modal solutions in layered, elastic media at high frequencies: Bull. Seis. Soc. Am., **55**, 335–358.
Farrell, W. E., 1972, Deformation of the earth by surface loads: Rev. Geophys. Space Phys., **10**, 761–797.
Garbesi, K., 1993, Toward resolving model-measurement discrepancies of radon entry into houses: Ph.D. thesis, Univ. of California, Berkeley.
Geertsma, J., 1973, Land subsidence above compacting oil and gas reservoirs: J. Petr. Tech., **25**, 734–744.
Grasso, J. R., 1992, Mechanics of seismic instabilities induced by the recovery of hydrocarbons: Pure Appl. Geophys., **139**, 506–534.
Hart, R. D., and John, C. M. S., 1986, Formulation of a fully-coupled thermal-mechanical-fluid flow model for non-linear geologic systems: Internat. J. Rock Mech. Min. Sci., **23**, 213–224.
Haskell, A., 1953, The dispersion of surface waves on multilayered media: Bul. Seis. Soc. Am., **43**, 17–34.
Jovanovich, D. B., Husseini, M. I., and Chinnery, M. A., 1974, Elastic dislocations in a layered half-space—I, Basic theory and numerical methods: Geophys. J. Roy. Astr. Soc., **39**, 205–217.
Kennett, B. L. N., 1983, Seismic wave propagation in stratified media: Cambridge Univ. Press.
Kim, J.-M., and Parizek, R., 1997, Numerical simulation of the Noordbergum effect resulting from groundwater pumping in a layered aquifer system: J. Hydrol., **202**, 231–243.
Knopoff, L., 1964, A matrix method for elastic wave problems.: Bull. Seis. Soc. Am., **54**, 431–438.
Kümpel, H.-J., 1982, Neigungsmessungen zwischen Hydrologie und Ozeanographie: Ph.D. thesis, Univ. of Kiel, Germany.
———1989, Verformungen in der Umgebung von Brunnen: Habil. thesis, Univ. of Kiel, Germany.
———1991, Poroelasticity—Parameters reviewed: Geophys. J. Internat., **105**, 783–799.
———1997, In situ deformation measurements for evaluation of hydraulic rock parameters, *in* Wang, S., and Marinos, P., Eds., Engineering Geology: Proc. 30th Internat. Geol. Congr., B. **23**, 481–487.
Kümpel, H.-J., Varga, P., Lehmann, K., and Mentes, G., 1996, Ground tilt induced by pumping—Preliminary results from the test site Nagycenk, Hungary: Acta Geod. Geoph. Hung., **31**, 67–78.
Lehmann, K., 2001, Porendruckinduzierte Neigungssignale in geringen Tiefen und ihre Modellierung im homogenen Halbraum: Ph.D. thesis, Univ. Bonn, Germany.
Lewis, R. W., and Schreffler, B. A., 1987, The finite element method in the deformation and consolidation of porous media: John Wiley & Sons, Inc.
Maruyama, T., 1994, Fluid pressure responses of a water-saturated porous elastic multi-layered half-space to water pumping and atmospheric loading: J. Phys. Earth, **42**, 331–375.
Okada, Y., 1992, Internal deformation due to shear and tensile faults in a half-space: Bull. Seis. Soc. Am., **82**, 1018–1040.
Rice, J. R., and Cleary, M. P., 1976, Some basic stress diffusion solutions for fluid-saturated elastic porous media with compressible constituents: Rev. Geophys. Space Phys., **14**, 227–241.
Roeloffs, E. A., 1988, Hydrologic precursors to earthquakes: A review: Pure Appl. Geophys., **126**, 177–209.
———1996, Poroelastic techniques in the study of earthquake related hydrologic phenomena: Adv. Geophys., **37**, 135–195.
Rudnicki, J. W., 1986, Fluid mass sources and point forces in linear elastic diffusive solids: Mech. Mat., **5**, 383–393.
Segall, P., 1985, Stresses and subsidence resulting from subsurface fluid withdrawal in the epicentral region of the 1983 Coalinga earthquake: J. Geophys. Res., **90**, 6801–6816.
Thomson, W. T., 1950, Transmission of elastic waves through a stratified solid medium: J. Appl. Phys., **21**, 89–93.
Vasco, D. W., Karasaki, K., and Doughty, C., 2000, Using surface deformation to image reservoir dynamics: Geophysics, **65**, 132–147.
Verruijt, A., 1969, Elastic storage of aquifers, *in* de Wiest, R. J. M., Ed., Flow through porous media: Academic Press Inc., 331–376.
Wang, H. F., 1993, Quasi-static poroelastic parameters in rock and their geophysical applications: Pure Appl. Geophys., **141**, 269–286.
———2000, Theory of linear poroelasticity with applications to geomechanics and hydrogeology: Princeton Univ. Press.
Wang, R., 1999, A simple orthonormalization method for stable and efficient computation of Green's functions: Bull. Seis. Soc. Am., **89**, 733–741.
Weise, A., 1992, Neigungsmessungen in der Geodynamik—Ergebnisse von der 3-Komponenten-Station Metsähovi: Ph.D. thesis, Tech. Univ. Clausthal, Germany.
Wolfram, S., 1988, Mathematica, a system for doing mathematics by computer: Addison-Wesley Publ. Co.
Zimmerman, R. W., 1991, Compressibility of sandstones: Elsevier Science Publ. Co., Inc.

APPENDIX A
POROELASTIC LAYER MATRIX

The six column vectors of the poroelastic layer matrix $\mathbf{L}$ defined by equation (82) are

$$\begin{cases} L_{11} = 1 \\ L_{21} = 2\mu k \\ L_{31} = 1 \\ L_{41} = 2\mu k \\ L_{51} = 0 \\ L_{61} = 0 \end{cases}, \tag{A-1}$$

$$\begin{cases} L_{12} = 1 \\ L_{22} = -2\mu k \\ L_{32} = -1 \\ L_{42} = 2\mu k \\ L_{52} = 0 \\ L_{62} = 0 \end{cases}, \tag{A-2}$$

$$\begin{cases} L_{13} = 1 + \frac{\eta_1}{\mu}(1 - kz) \\ L_{23} = 2\eta_1(1 - kz)k \\ L_{33} = -1 - \frac{\eta_1}{\mu}kz \\ L_{43} = -2\eta_1 k^2 z \\ L_{53} = -2\alpha Qk \\ L_{63} = 2\alpha\chi Qk^2 \end{cases}, \tag{A-3}$$

$$\begin{cases} L_{14} = 1 + \frac{\eta_1}{\mu}(1 + kz) \\ L_{24} = -2\eta_1(1 + kz)k \\ L_{34} = 1 - \frac{\eta_1}{\mu}kz \\ L_{44} = 2\eta_1 k^2 z \\ L_{54} = 2\alpha Qk \\ L_{64} = 2\alpha\chi Qk^2 \end{cases}, \tag{A-4}$$

$$\begin{cases} L_{15} = \alpha \\ L_{25} = \frac{2\mu k^2 \alpha}{k_p} \\ L_{35} = \frac{k\alpha}{k_p} \\ L_{45} = 2\mu k\alpha \\ L_{55} = \frac{\zeta s}{\beta k_p} \\ L_{65} = -\frac{\chi\zeta s}{\beta} \end{cases}, \tag{A-5}$$

$$\begin{cases} L_{16} = \alpha \\ L_{26} = -\frac{2\mu k^2 \alpha}{k_p} \\ L_{36} = -\frac{k\alpha}{k_p} \\ L_{46} = 2\mu k\alpha \\ L_{56} = -\frac{\zeta s}{\beta k_p} \\ L_{66} = -\frac{\chi\zeta s}{\beta} \end{cases}, \tag{A-6}$$

where

$$\beta = \frac{\chi\zeta Q}{\zeta_1}, \tag{A-7}$$

$$\eta_1 = \eta + \alpha^2 Q. \tag{A-8}$$

The six row vectors of the inverse layer matrix $\mathbf{L}^{-1}$ are

$$\begin{cases} (L^{-1})_{11} = \frac{-2\alpha^2\beta\mu Qk^2 + \zeta\eta_1 s - \zeta\eta_1 s(1 - kz)}{2\zeta\zeta_1 s} \\ (L^{-1})_{12} = \frac{-2\alpha^2 Q\beta\mu k^2 + \zeta\zeta_1 s - \zeta\eta_1(1 - kz)s}{4\mu\zeta\zeta_1 ks} \\ (L^{-1})_{13} = \frac{2\alpha^2 Q\beta\mu k^2 + \zeta\eta_1(1 - kz)s}{2\zeta\zeta_1 s} \\ (L^{-1})_{14} = \frac{2\alpha^2 Q\beta\mu k^2 + \zeta\mu s + \zeta\eta_1(1 - kz)s}{4\mu\zeta\zeta_1 ks} \\ (L^{-1})_{15} = -\frac{\alpha\beta k}{2\zeta s} \\ (L^{-1})_{16} = \frac{\alpha Q}{2\zeta_1 s} \end{cases}, \tag{A-9}$$

$$\begin{cases} (L^{-1})_{21} = \frac{-2\alpha^2 Q\beta\mu k^2 + \zeta\eta_1 s - \zeta\eta_1 s(1 + kz)}{2\zeta\zeta_1 s} \\ (L^{-1})_{22} = \frac{2\alpha^2 Q\beta\mu k^2 - \zeta\zeta_1 s + \zeta\eta_1(1 + kz)s}{4\mu\zeta\zeta_1 ks} \\ (L^{-1})_{23} = \frac{-2\alpha^2 Q\beta\mu k^2 - \zeta\eta_1(1 + kz)s}{2\zeta\zeta_1 s} \\ (L^{-1})_{24} = \frac{2\alpha^2 Q\beta\mu k^2 + \zeta\mu s + \zeta\eta_1(1 + kz)s}{4\mu\zeta\zeta_1 ks} \\ (L^{-1})_{25} = \frac{\alpha\beta k}{2\zeta s} \\ (L^{-1})_{26} = \frac{\alpha Q}{2\zeta_1 s} \end{cases}, \tag{A-10}$$

$$\begin{cases} (L^{-1})_{31} = \dfrac{\mu}{2\zeta_1} \\ (L^{-1})_{32} = \dfrac{1}{4\zeta_1 k} \\ (L^{-1})_{33} = -\dfrac{\mu}{2\zeta_1} \\ (L^{-1})_{34} = -\dfrac{1}{4\zeta_1 k} \\ (L^{-1})_{35} = 0 \\ (L^{-1})_{36} = 0 \end{cases}, \tag{A-11}$$

$$\begin{cases} (L^{-1})_{41} = \dfrac{\mu}{2\zeta_1} \\ (L^{-1})_{42} = -\dfrac{1}{4\zeta_1 k} \\ (L^{-1})_{43} = \dfrac{\mu}{2\zeta_1} \\ (L^{-1})_{44} = -\dfrac{1}{4\zeta_1 k} \\ (L^{-1})_{45} = 0 \\ (L^{-1})_{46} = 0 \end{cases}, \tag{A-12}$$

$$\begin{cases} (L^{-1})_{51} = \dfrac{\alpha Q\beta\mu k^2}{\zeta\zeta_1 s} \\ (L^{-1})_{52} = \dfrac{\alpha Q\beta k_p}{2\zeta\zeta_1 s} \\ (L^{-1})_{53} = -\dfrac{\alpha Q\beta\mu k k_p}{\zeta\zeta_1 s} \\ (L^{-1})_{54} = -\dfrac{\alpha Q\beta k}{2\zeta\zeta_1 s} \\ (L^{-1})_{55} = \dfrac{\beta k_p}{2\zeta s} \\ (L^{-1})_{56} = -\dfrac{Q}{2\zeta_1 s} \end{cases}, \tag{A-13}$$

$$\begin{cases} (L^{-1})_{61} = \dfrac{\alpha Q\beta\mu k^2}{\zeta\zeta_1 s} \\ (L^{-1})_{62} = -\dfrac{\alpha Q\beta k_p}{2\zeta\zeta_1 s} \\ (L^{-1})_{63} = \dfrac{\alpha Q\beta\mu k k_p}{\zeta\zeta_1 s} \\ (L^{-1})_{64} = -\dfrac{\alpha Q\beta k}{2\zeta\zeta_1 s} \\ (L^{-1})_{65} = -\dfrac{\beta k_p}{2\zeta s} \\ (L^{-1})_{66} = -\dfrac{Q}{2\zeta_1 s} \end{cases}. \tag{A-14}$$

APPENDIX B

HASKELL'S PROPAGATOR ALGORITHM

Haskell's propagator algorithm for solving the poroelastic boundary value problem based on the layered half-space model is demonstrated by the following program-ready procedure.

First, define three vector bases at the surface ($z = z_1 = 0$), which can be orthonormal but need not to be so; for example,

$$\mathbf{Y}^{(1)} = \mathbf{Y}^{(c)} = \left(\mathbf{y}_1^{(c)}, \mathbf{y}_2^{(c)}, \mathbf{y}_3^{(c)} \right) = \begin{pmatrix} 1 & 0 & 0 \\ 0 & 0 & 0 \\ 0 & 1 & 0 \\ 0 & 0 & 0 \\ 0 & 0 & 0 \\ 0 & 0 & 1 \end{pmatrix}. \tag{B-1}$$

Decompose the surface displacement vector as

$$\mathbf{y}(z_1) = U\,\mathbf{y}_1^{(c)} + V\,\mathbf{y}_2^{(c)} + P\,\mathbf{y}_3^{(c)}, \tag{B-2}$$

where U, V, and P are constants to be determined. For the $\mathbf{Y}^{(c)}$, they are exactly the desired poloidal solutions for U_m, V_m, P_m at the surface, respectively. Similarly, define the vector bases at the lowest interface, that is, at the top of the homogeneous half-space ($z = z_n$):

$$\mathbf{Y}^{(n)} = \left(\mathbf{y}_1^{(n)}, \mathbf{y}_2^{(n)}, \mathbf{y}_3^{(n)} \right) = \mathbf{L}_n(0) \cdot \mathbf{C}, \tag{B-3}$$

where

$$\mathbf{C} = \begin{pmatrix} 0 & 0 & 0 \\ 1 & 0 & 0 \\ 0 & 0 & 0 \\ 0 & 1 & 0 \\ 0 & 0 & 0 \\ 0 & 0 & 1 \end{pmatrix}. \tag{B-4}$$

Decompose the displacement vector as

$$\mathbf{y}(z_n) = A^-\,\mathbf{y}_1^{(n)} + B^-\,\mathbf{y}_2^{(n)} + C^-\,\mathbf{y}_3^{(n)}. \tag{B-5}$$

Note that there are only *downgoing waves* in the half-space.

Second, assuming that the source plane $z = z_s$ lies above the half-space, propagate $\mathbf{Y}$ from the surface $z = 0$ and from the top of the half-space $z = z_n$ to the source plane with $\mathbf{Y}^{(c)}$ and $\mathbf{Y}^{(n)}$ as the starting values, respectively, via the chain rules

$$\mathbf{Y}^{(i)} = \mathbf{H}_i(h_i)\mathbf{Y}^{(i-1)}, \quad \text{for } z_i \le z_s^-, \tag{B-6}$$

$$\mathbf{Y}^{(i)} = \mathbf{H}_i(-h_i)\mathbf{Y}^{(i+1)}, \quad \text{for } z_i \ge z_s^+, \tag{B-7}$$

where h_i is the thickness of the ith layer and where z_s^- and z_s^+ are the upper and lower sides of the source plane, respectively. For simplicity, they are treated as two different pseudointerfaces z_s and z_{s+1} in the next step.

Third, find the decomposition constants $\{U, V, P\}$ and $\{A^-, B^-, C^-\}$ by the source condition

$$A^- \mathbf{y}_1^{(s+1)} + B^- \mathbf{y}_2^{(s+1)} + C^- \mathbf{y}_3^{(s+1)} = U \mathbf{y}_1^{(s)} + V \mathbf{y}_2^{(s)} + P \mathbf{y}_3^{(s)} + \Delta \mathbf{y}(z_s), \tag{B-8}$$

where $\Delta \mathbf{y}(z_s)$ is the source function vector. The global displacement vectors are finally given by

$$\mathbf{y}(z_i) = \begin{cases} U \mathbf{y}_1^{(i)} + V \mathbf{y}_2^{(i)} + P \mathbf{y}_3^{(i)}, \\ \quad \text{for } z_i = z_1, \ldots, z_s; \\ A^- \mathbf{y}_1^{(i)} + B^- \mathbf{y}_2^{(i)} + C^- \mathbf{y}_3^{(i)}, \\ \quad \text{for } z_i = z_{s+1}, \ldots, z_n. \end{cases} \tag{B-9}$$

APPENDIX C

THE ORTHONORMALIZED PROPAGATOR ALGORITHM

To avoid the numerical difficulty of the original Haskell's propagator algorithm, we insert an additional orthonormalization procedure in the iteration loop. The following program-ready procedure demonstrates this extension for a propagation from the free surface to the source plane.

First, start with

$$\mathbf{Y}^{(i)} = \mathbf{Y}^{(c)}. \tag{C-1}$$

Next, determine the corresponding constant coefficient vectors $\mathbf{C}$ for the ith layer by solving

$$\mathbf{C} = \mathbf{L}_i^{-1}(0) \cdot \mathbf{Y}^{(i)}. \tag{C-2}$$

Third, normalize $\mathbf{C}$ and, if the global solutions for all depths are requested, normalize all $\mathbf{Y}^{(j)}$ $(j = 1, \ldots, i)$ for the interfaces that have been passed, that is,

$$\mathbf{C} := \mathbf{C} \cdot \mathbf{N}, \tag{C-3}$$

$$\mathbf{Y}^{(j)} := \mathbf{Y}^{(j)} \cdot \mathbf{N}, \quad \text{for } j = 1, \ldots, i, \tag{C-4}$$

where ':=' denotes reset to and $\mathbf{N}$ is the normalization matrix

$$\mathbf{N} = dia(|\mathbf{c}_1|^{-1}, |\mathbf{c}_2|^{-1}, |\mathbf{c}_3|^{-1}). \tag{C-5}$$

Here $\mathbf{c}^{(j)}$ $(j = 1, 2, 3)$ are the three column vectors of $\mathbf{C}$. This step is necessary to avoid overflow and loss of precision resulting from operations between values of different orders in the next step.

Fourth, define a 3×3 manipulation matrix:

$$\mathbf{M} = \mathbf{C}_1^{-1}, \tag{C-6}$$

where $\mathbf{C}_1$ is the submatrix of $\mathbf{C}$ consisting of rows 1, 3, and 5, which are related to the three positive exponentials, respectively. Reconstruct the vector bases as

$$\mathbf{C} := \mathbf{C} \cdot \mathbf{M}, \tag{C-7}$$

$$\mathbf{Y}^{(j)} := \mathbf{Y}^{(j)} \cdot \mathbf{M}, \quad \text{for } j = 1, \ldots, i. \tag{C-8}$$

After this step, the submatrix becomes a 3×3 unit matrix (orthogonalized). Accordingly, for the ith layer the three different incident upgoing waves, whose amplitudes may increase quite differently with depth, will each be included individually in the three vector bases.

Finally, propagate the vector bases to the next interface by solving

$$\mathbf{Y}^{(i+1)} = \mathbf{L}_i(h_i) \cdot \mathbf{E}_i(h_i) \cdot \mathbf{C}. \tag{C-9}$$

Numerical coupling between the incident upgoing waves is avoided, so the loss-of-precision problem is solved regardless how thick a layer may be.

The propagation from the half-space upward to the source plane can be done using an analog method. The only difference is that the vector bases will be orthogonalized with respect to the downgoing waves and the thickness parameter h_i is replaced by $-h_i$.